Supporting Information

Iridium-Based Multimetallic Nanoframe@Nanoframe Structure: An Efficient and Robust Electrocatalyst toward Oxygen Evolution Reaction

Jongsik Park,[†,§,‡] *Young Jin Sa,*[∥,‡] *Hionsuck Baik,*[⊥] *Taehyun Kwon,*[†,§] *Sang Hoon Joo,*[*,∥,#] *and Kwangyeol Lee*[*,†,§]

[†] Center for Molecular Spectroscopy and Dynamics, Institute for Basic Science (IBS), Seoul 02841, Korea

[§] Department of Chemistry and Research Institute for Natural Sciences, Korea University, Seoul 02841, Korea

[∥] Department of Chemistry and [#] School of Energy and Chemical Engineering, Ulsan National Institute of Science and Technology (UNIST), Ulsan 44919, Korea

[⊥] Korea Basic Science Institute (KBSI), Seoul 02841, Korea

[‡] These authors contributed equally.

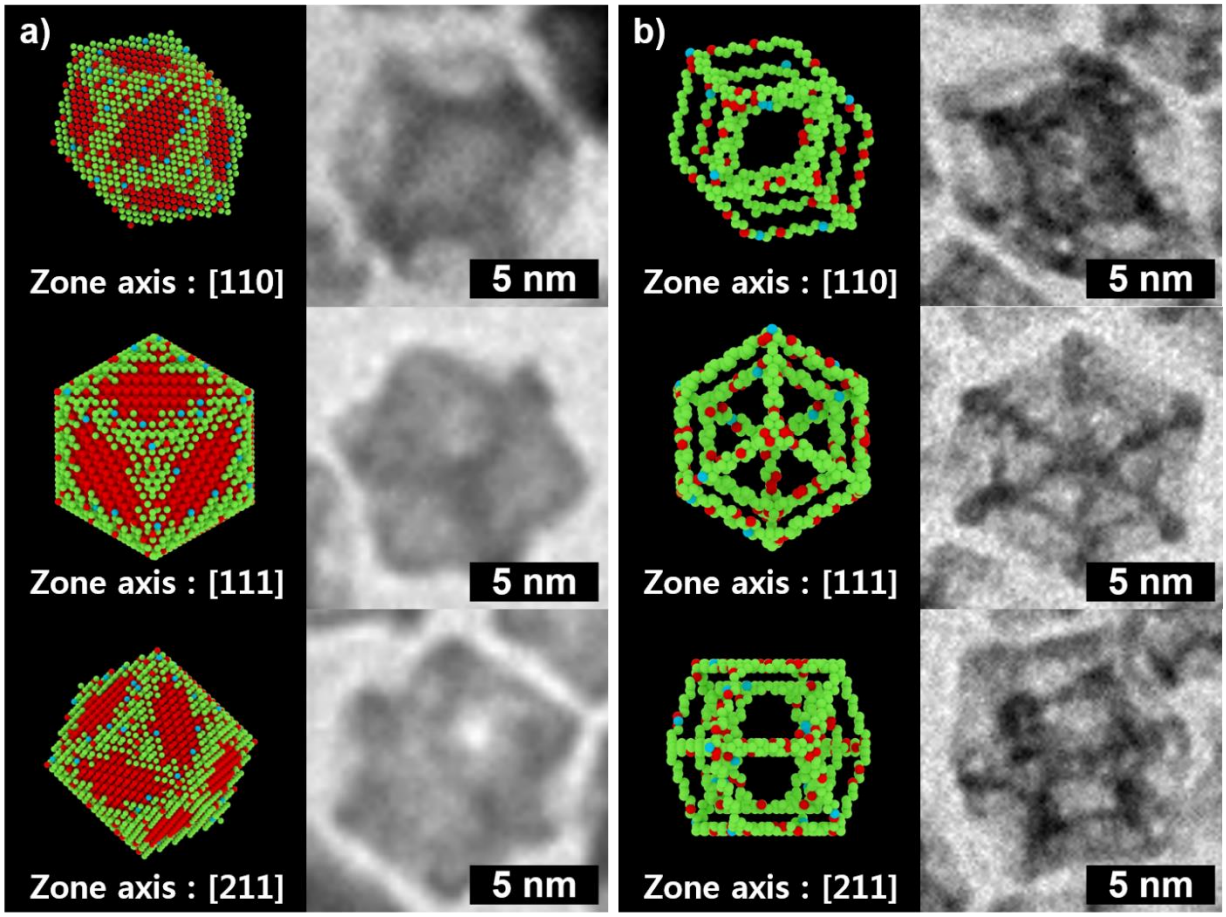

Figure S1. Structural models and corresponding TEM images viewed from different zone axes for (a) unetched DNF and (b) etched IrNiCu DNF.

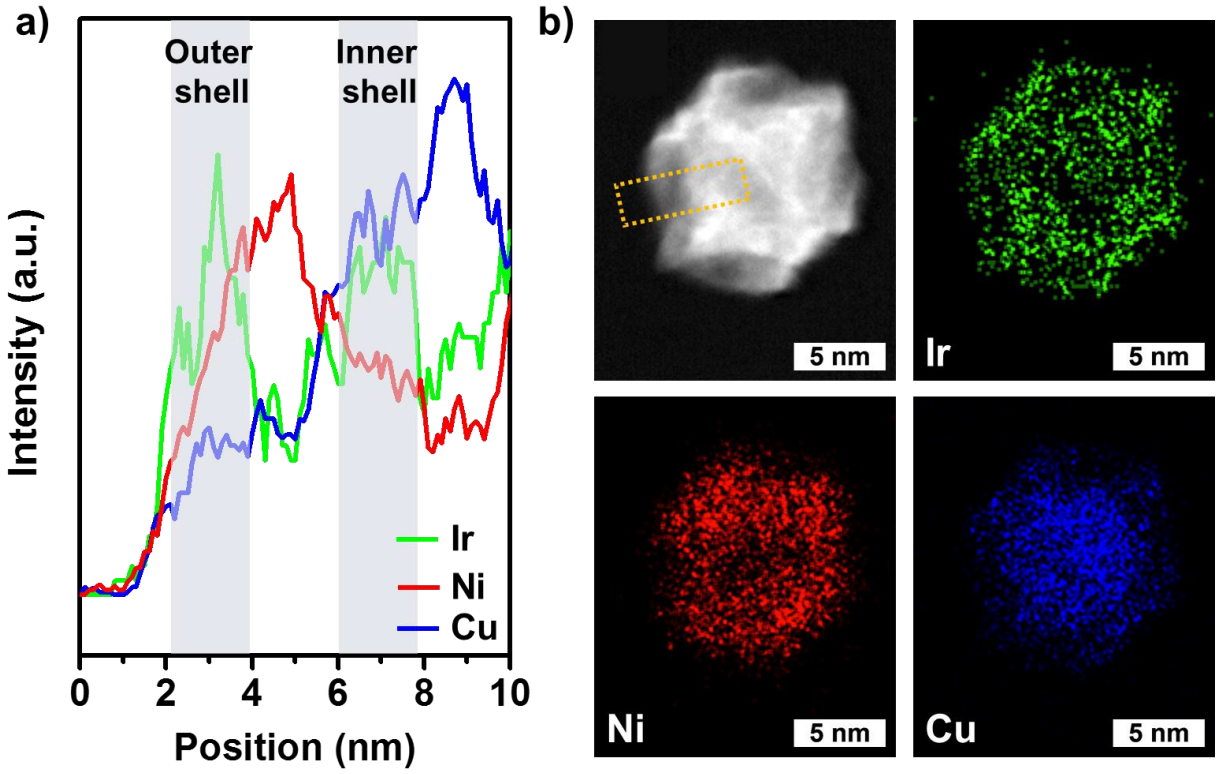

Figure S2. (a) Line profile data of unetched DNF. (b) HAADF-STEM image and corresponding elemental mapping analysis images of unetched DNF. Green, red, and blue colors are used to denote Ir, Ni, and Cu, respectively.

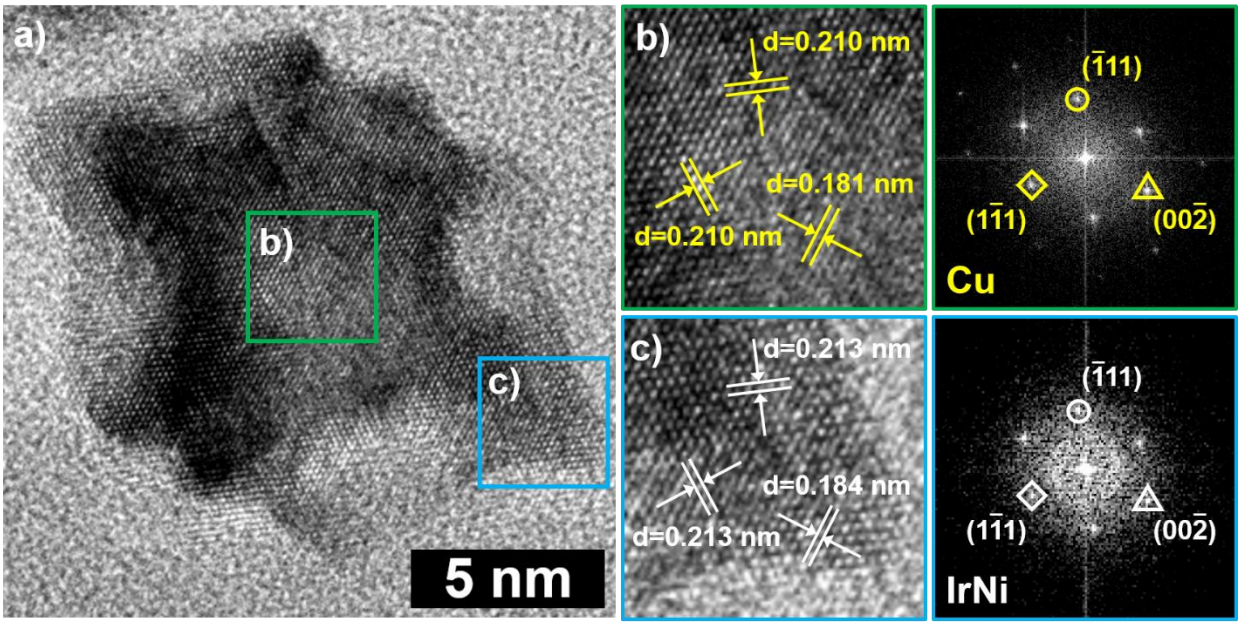

Figure S3. (a) HRTEM image of unetched DNF. (b) Enlarged HRTEM image of green square section in panel (a), and its FFT pattern. (c) Enlarged HRTEM image of blue square section in panel (a), and its FFT pattern. The zone axis of both images in (b) and (c) is [110].

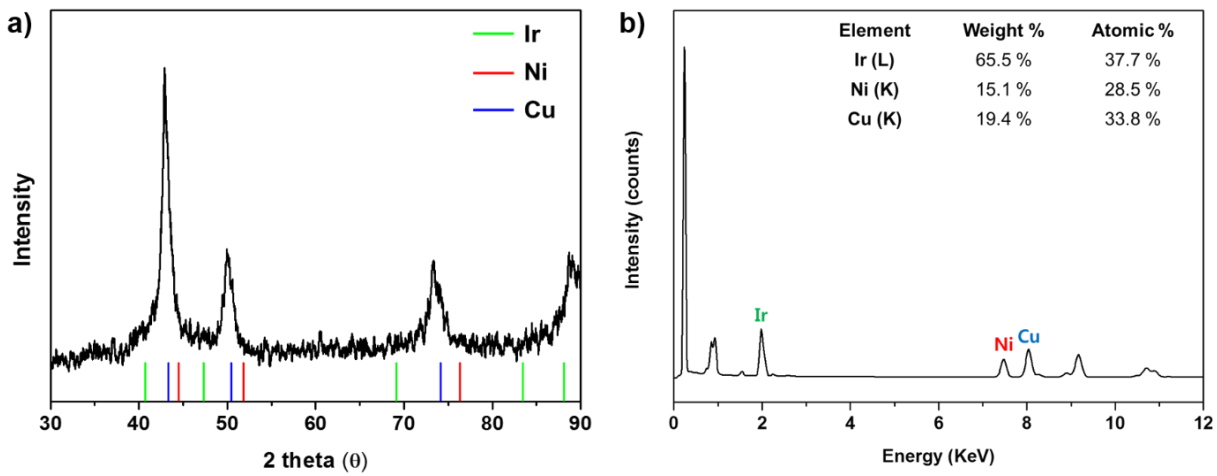

Figure S4. (a) PXRD pattern of unetched DNF. Standards for Ir (JCPDS 87-0715), Ni (JCPDS 71-4654), and Cu (JCPDS 85-1326) are also displayed. (b) EDS spectrum of unetched DNF. Sample for EDS measurement was prepared on a Mo TEM grid.

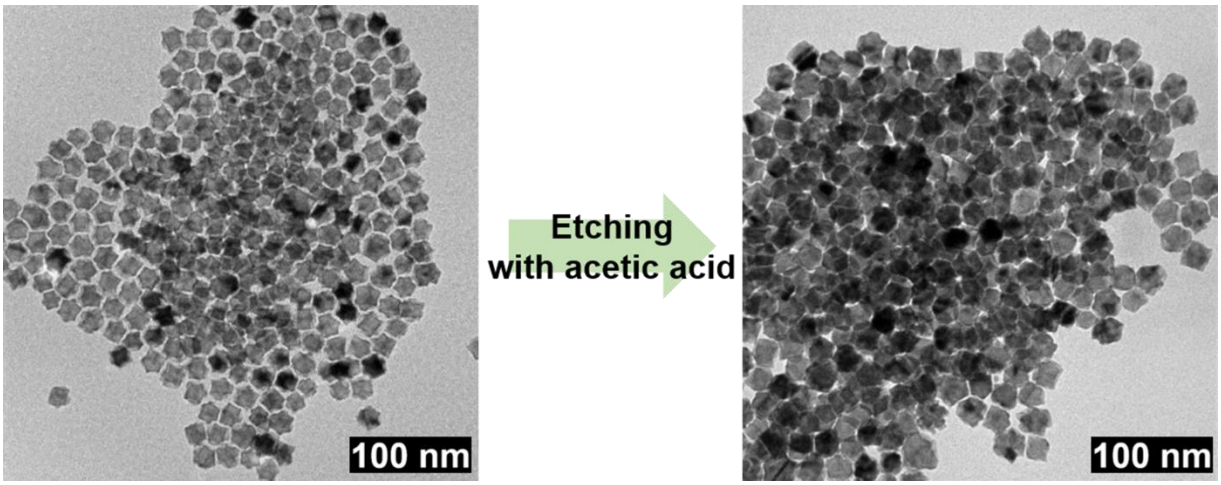

Figure S5. TEM images of unetched DNF before (left) and after (right) chemical etching with acetic acid.

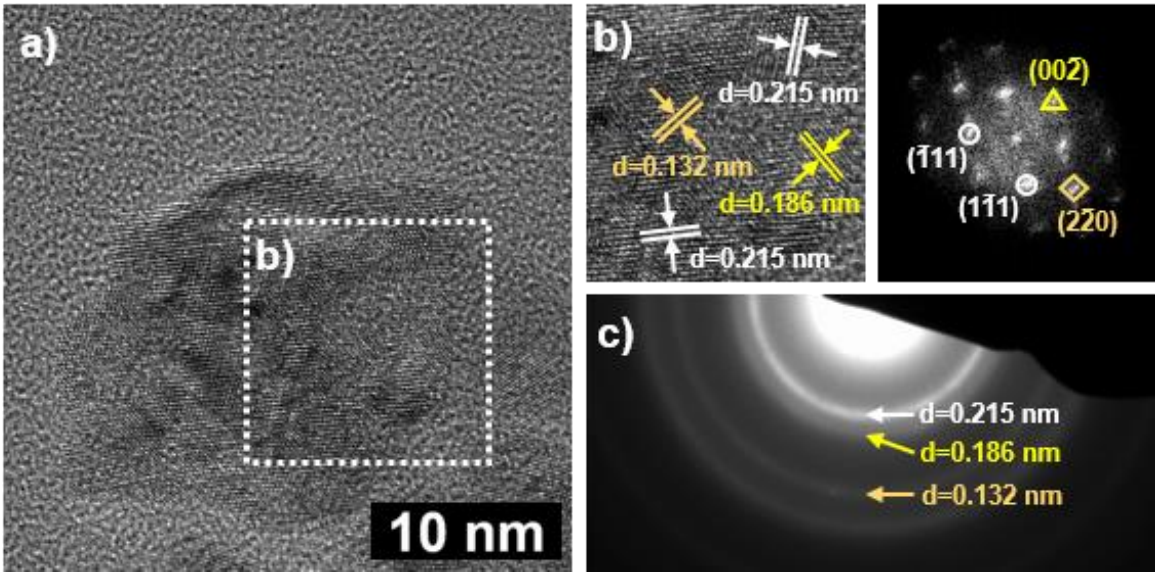

Figure S6. (a) HRTEM image of DNF. (b) Enlarged HRTEM of white dotted square section in panel (a), and its FFT pattern. (c) SAED pattern of DNF.

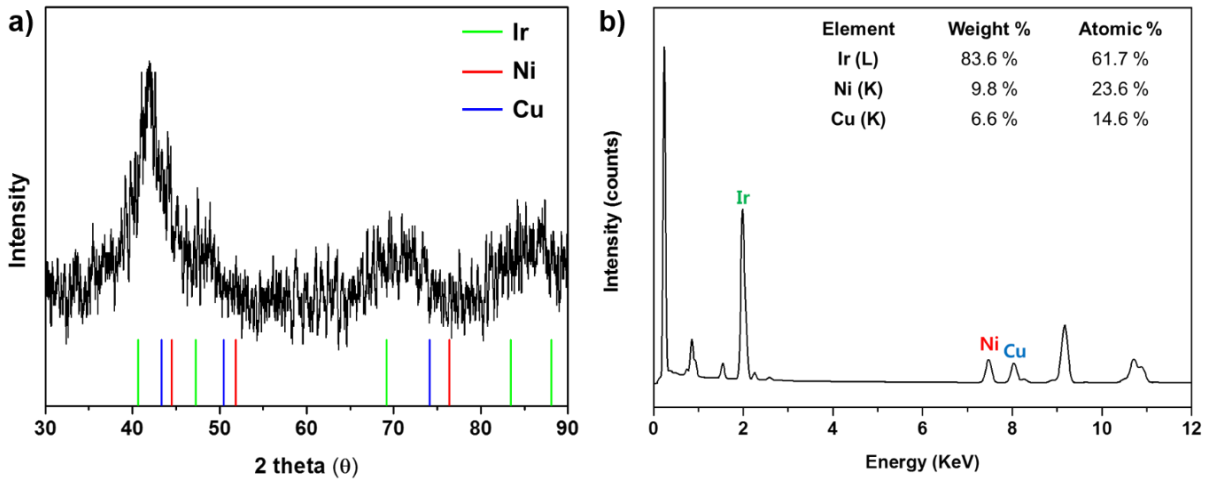

Figure S7. (a) PXRD pattern of DNF. Standards for Ir (JCPDS 87-0715), Ni (JCPDS 71-4654), and Cu (JCPDS 85-1326) are also displayed. (b) EDS spectrum of DNF. Sample for EDS measurement was prepared on a Mo TEM grid.

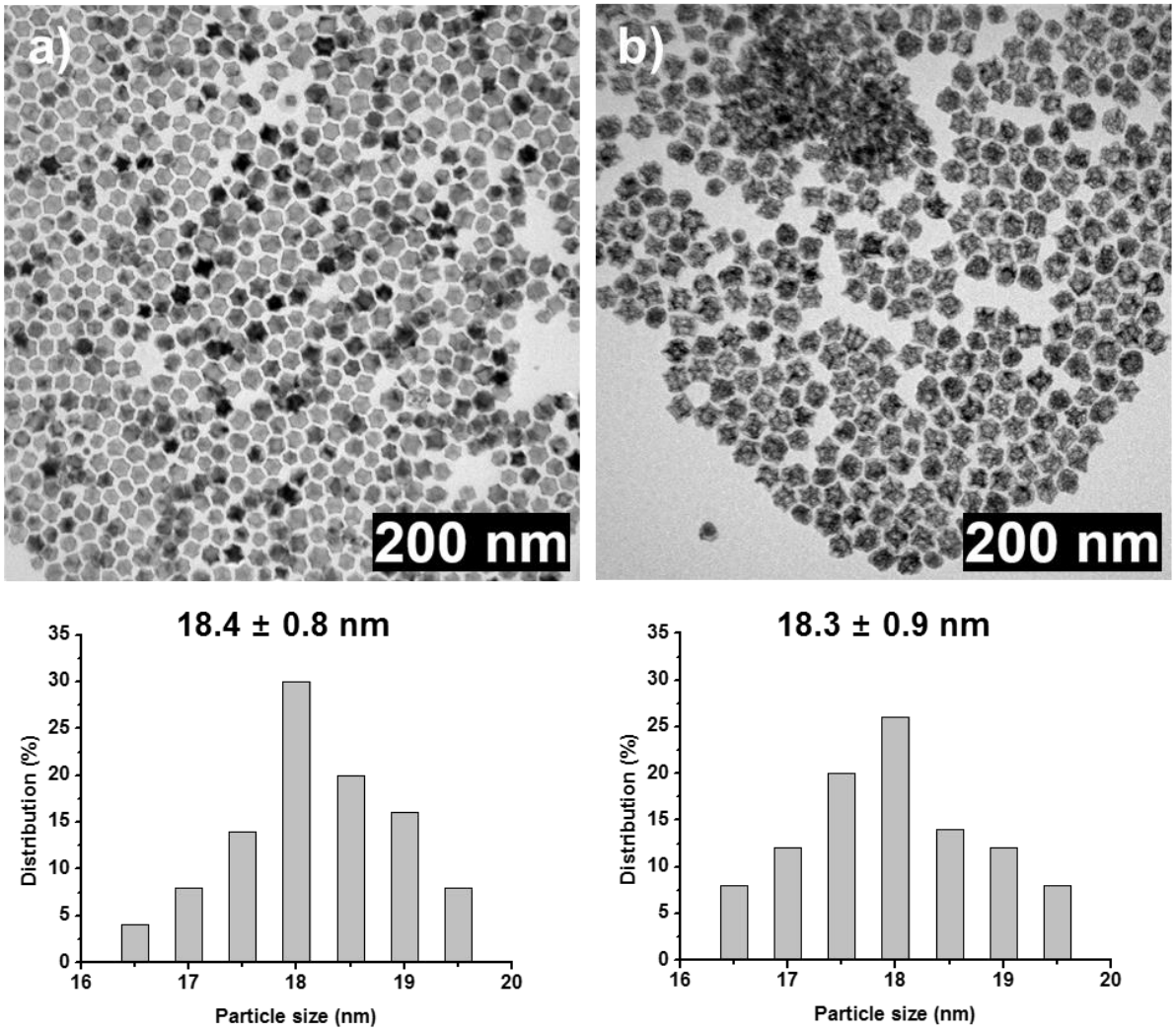

Figure S8. TEM images and histograms for crystal size distributions of (a) unetched DNF and (b) etched DNF. The size of nanocrystal remains unchanged after the chemical etching with HCl.

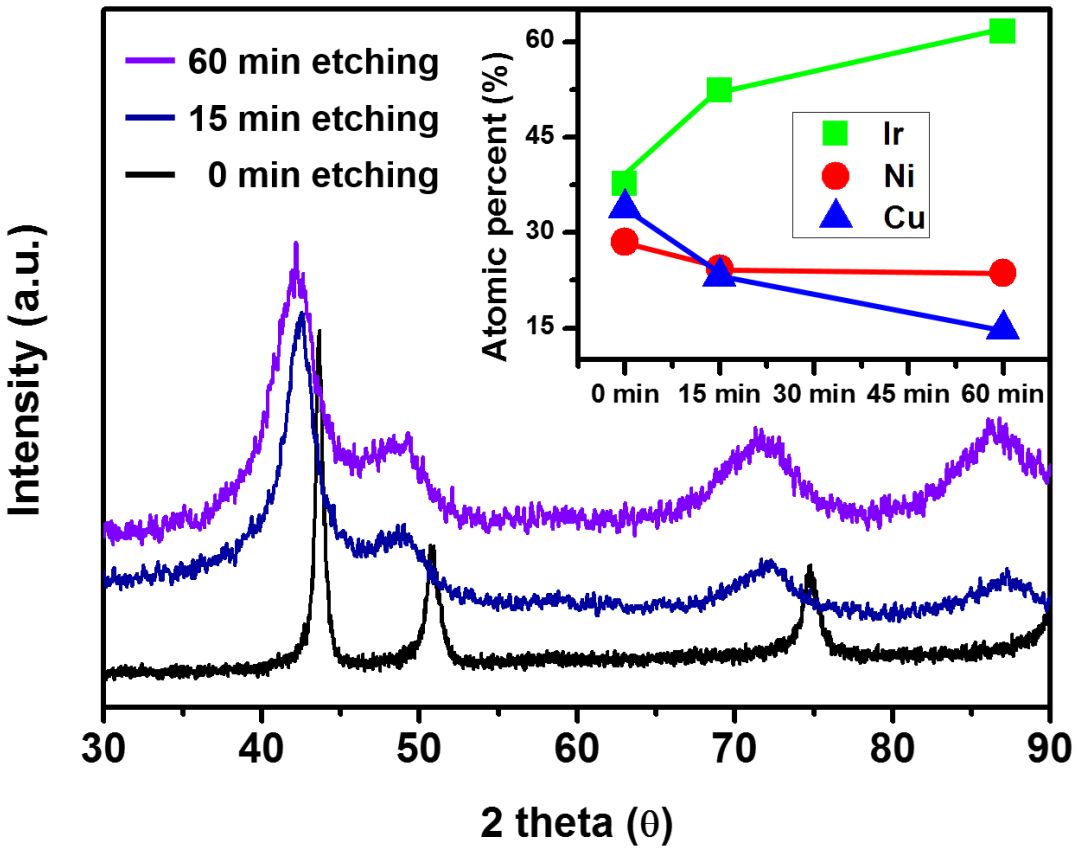

Figure S9. PXRD patterns and elemental analysis data, obtained by EDS spectra, of intermediates at different etching times; (a) before etching (0 min etching), (b) 15 min etching, and (c) 60 min etching, respectively.

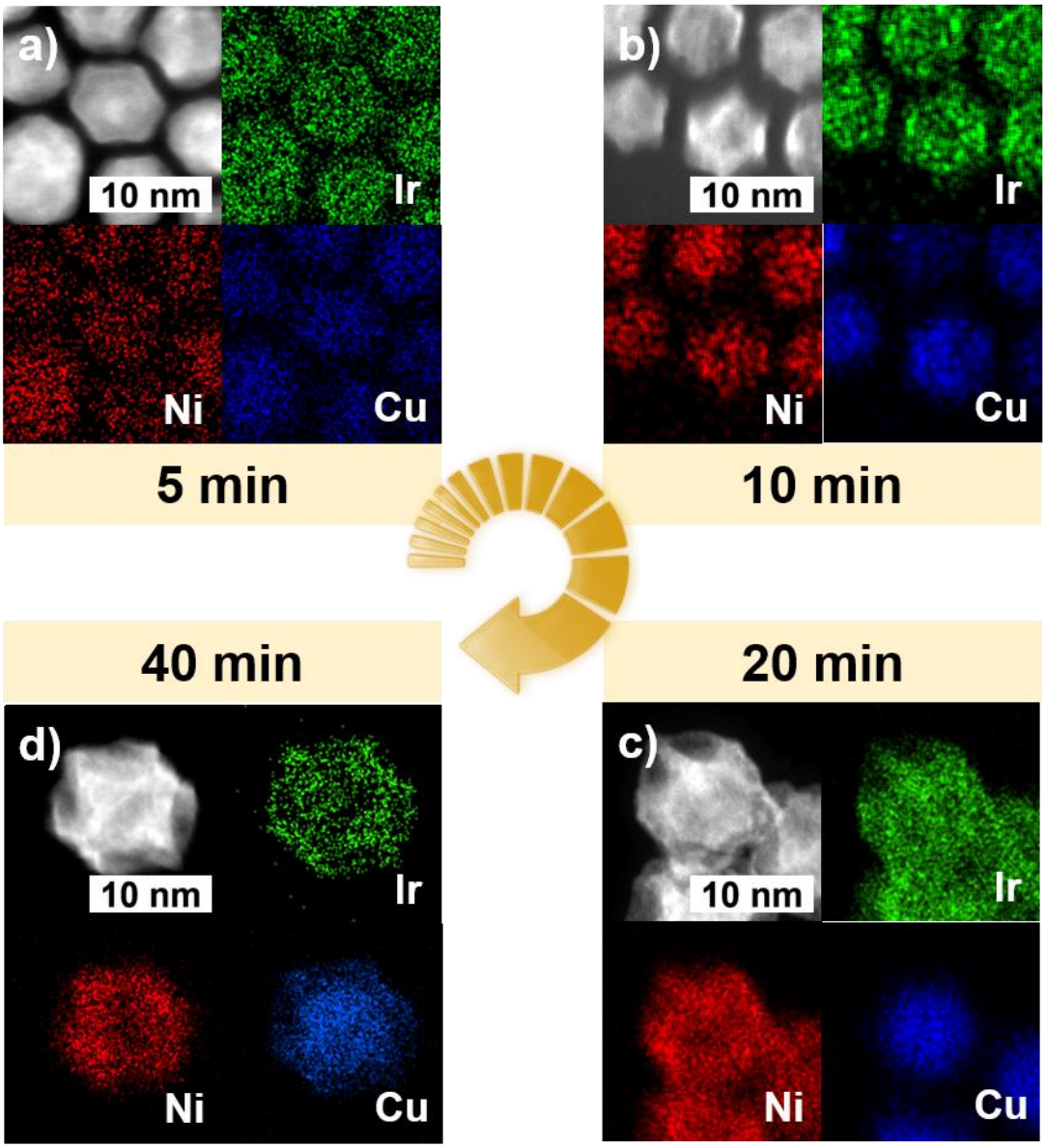

Figure S10. HAADF-STEM images and corresponding elemental mapping images of intermediates for unetched DNF at different reaction time: (a) 5 min, (b) 10 min, (c) 20 min, and (d) 40 min.

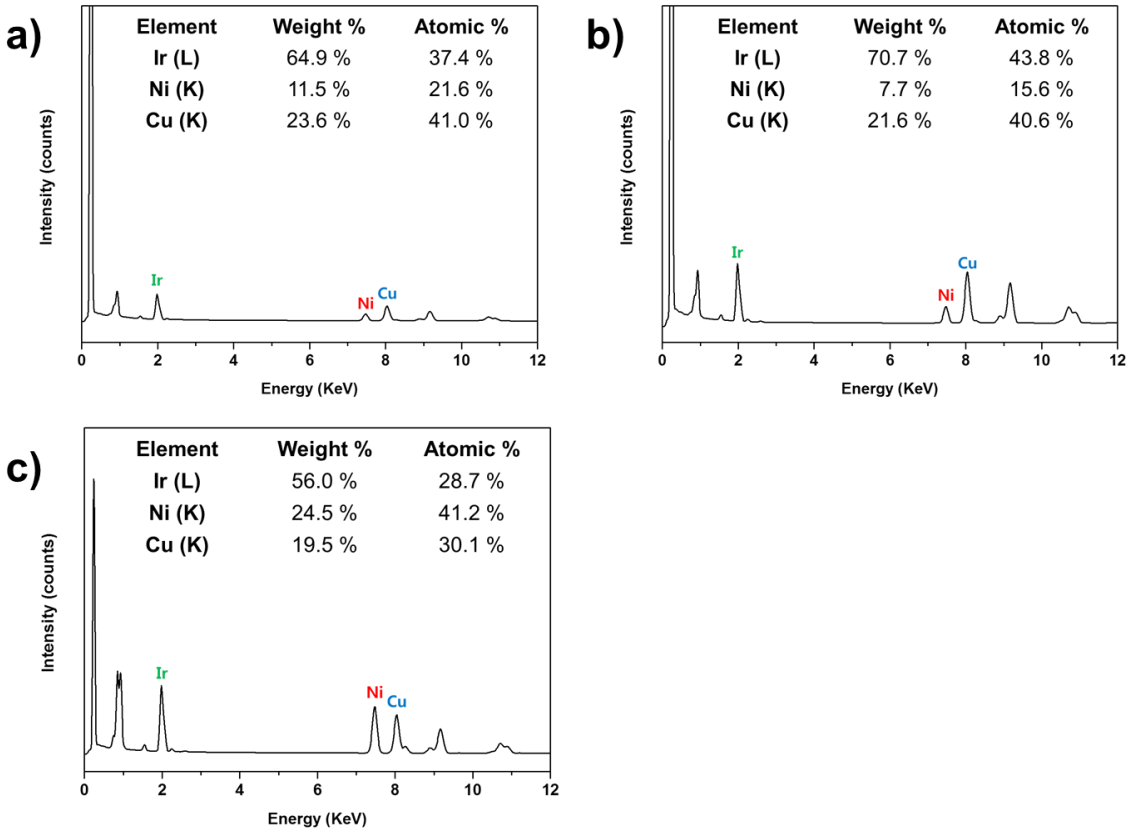

Figure S11. EDS spectra of intermediates for unetched DNF at different reaction times: (a) 5 min, (b) 10 min, and (c) 20 min.

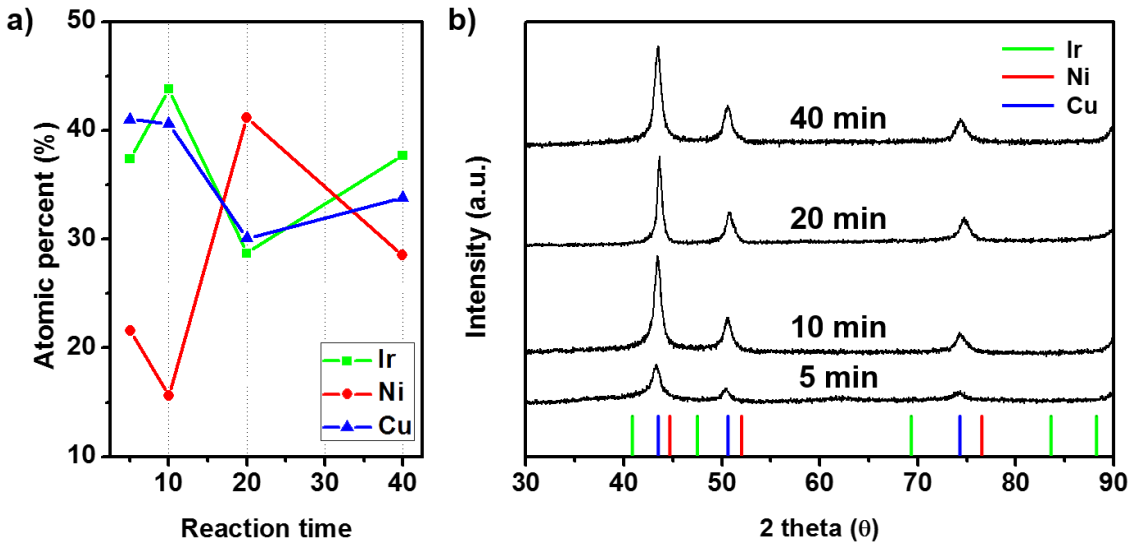

Figure S12. (a) Elemental analysis data obtained from EDS spectra of intermediates for unetched DNF. (b) PXRD patterns of intermediates for unetched DNF at different reaction times.

Table 1. Metal contents in IrNiCu DNF/C and IrNiCu SNF/C catalysts determined by ICP-OES analysis.

Sample	Weight Percent (%)			Atomic Percent (%)		
	Ir	Ni	Cu	Ir	Ni	Cu
IrNiCu DNF/C	12.5	1.3	0.3	70.8	24.1	5.1
IrNiCu SNF/C	15.3	1.3	0.3	74.8	20.8	4.4

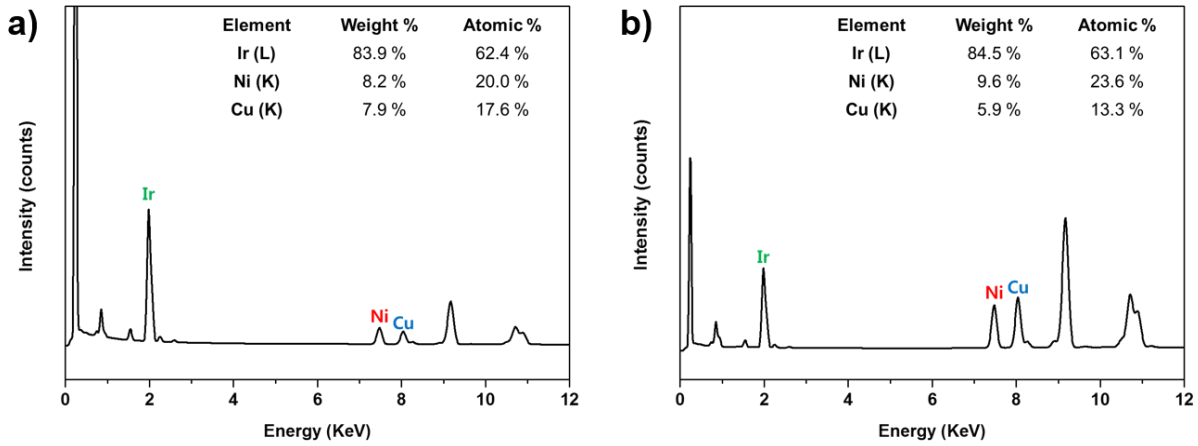

Figure S13. EDS spectra of IrNiCu SNF prepared using a single Ir precursor: (a) $Ir(acac)_3$ and (b) $IrCl_3$.

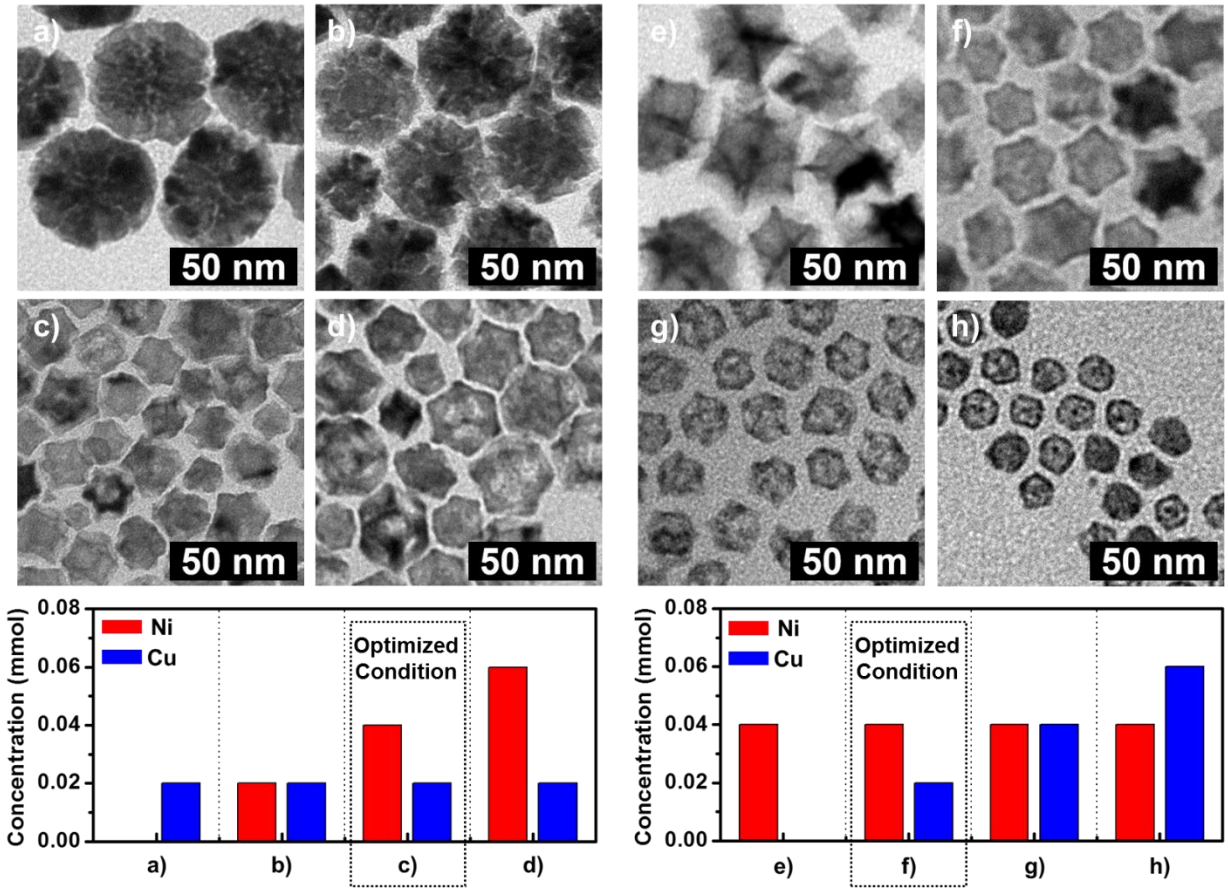

Figure S14. Effect of the concentration of Ni or Cu precursor on the morphology of unetched nanocrystals. (a–d) TEM images of unetched nanocrystals prepared from $Ni(acac)_2$ concentration of (a) 0 mmol, (b) 0.02 mmol, (c) 0.04 mmol, and (d) 0.06 mmol at a fixed $Cu(acac)_2$ concentration of 0.02 mmol. (e–g) TEM images of unetched nanocrystals prepared from $Cu(acac)_2$ concentration of (e) 0 mmol, (f) 0.02 mmol, (g) 0.04 mmol, and (h) 0.06 mmol at a fixed $Ni(acac)_2$ concentration of 0.04 mmol.

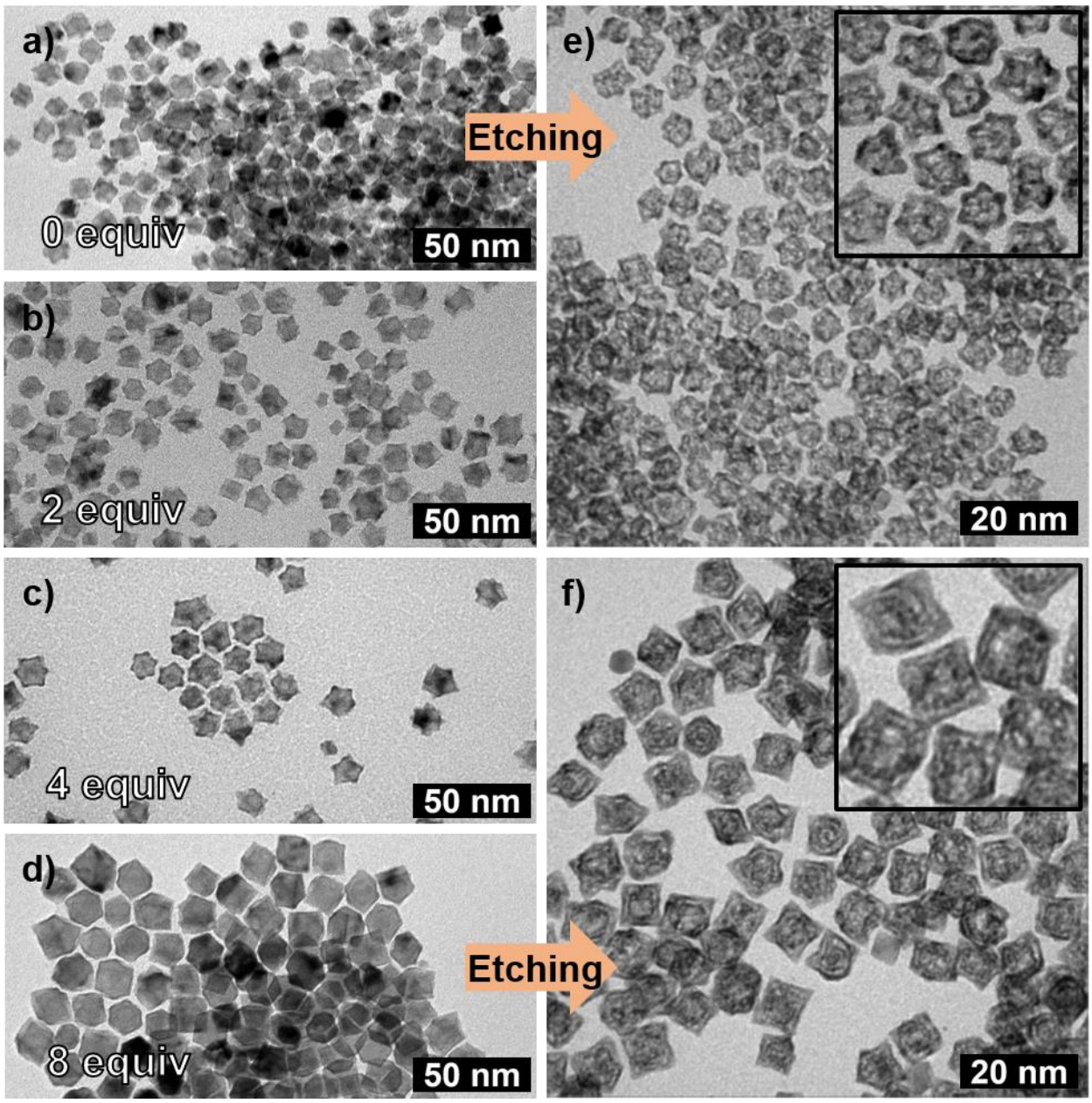

Figure S15. Effect of the amount of reducing agent (1,2-HDD) on the morphology of unetched nanocrystals. (a–d) TEM images of unetched nanocrystals prepared from 1,2-HDD amount of (a) 0 equiv, (b) 2 equiv, (c) 4 equiv, and (d) 8 equiv. (e,f) TEM images of etched nanocrystals prepared from (e) 0 equiv and (f) 8 equiv conditions.

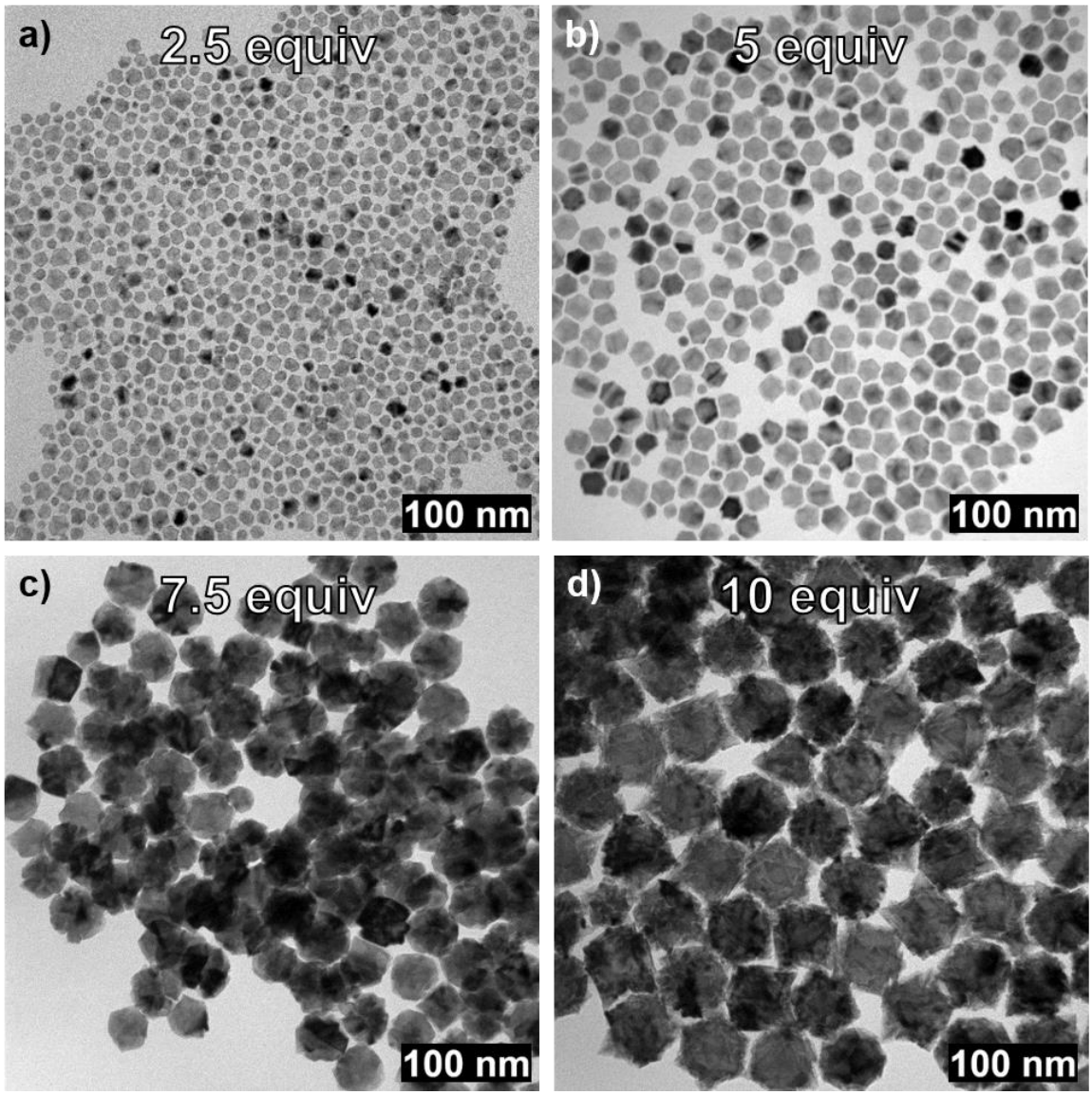

Figure S16. Effect of the amount of CTAC surfactant on the morphology of unetched nanocrystals. (a–d) TEM images of unetched nanocrystals prepared from CTAC amount of (a) 2.5 equiv, (b) 5 equiv, (c) 7.5 equiv, and (d) 10 equiv.

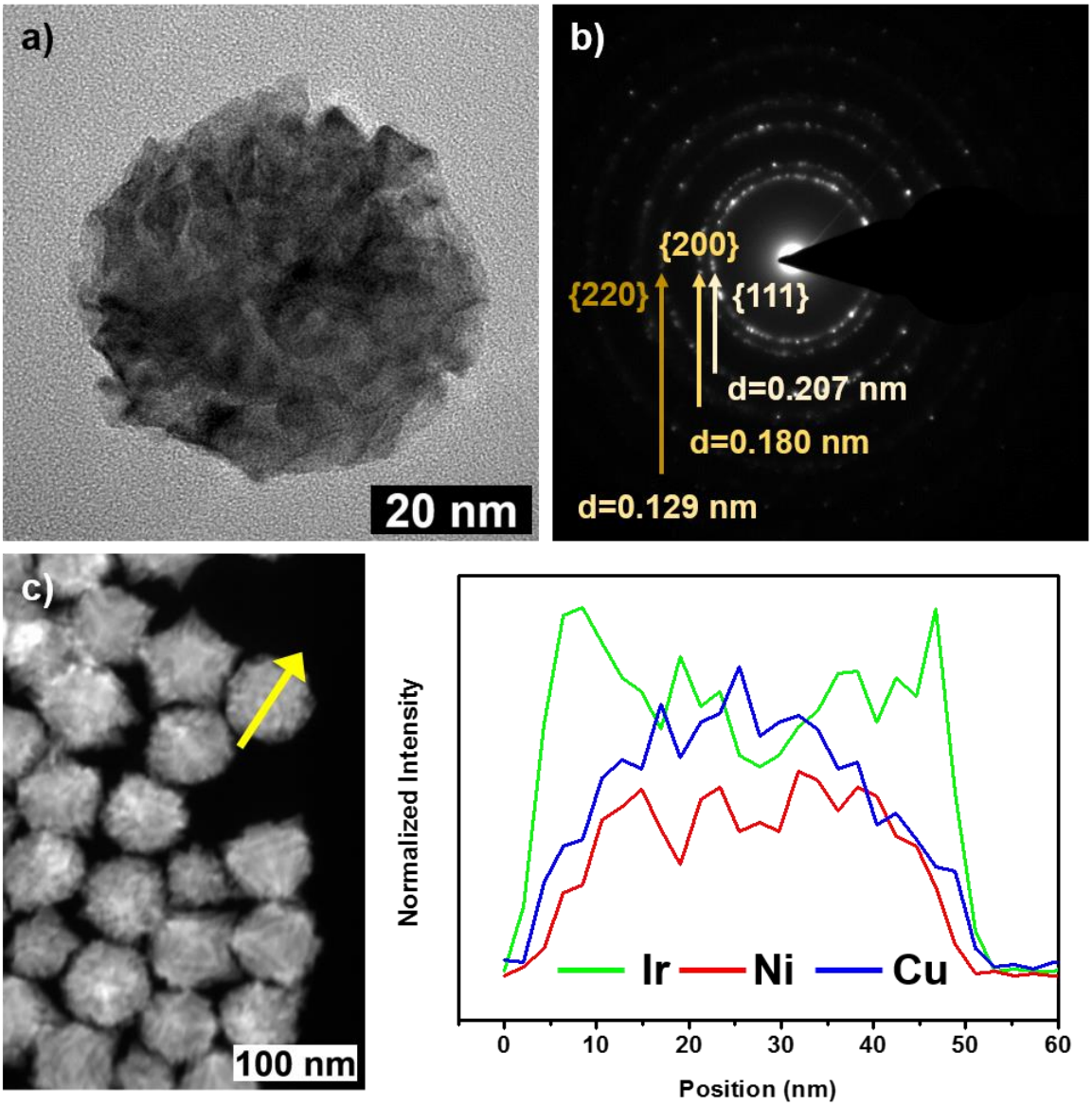

Figure S17. Characterization of hierarchical CuNi@Ir core-shell nanostructures (Figure S16d) after chemical etching. (a) TEM image and (b) SAED pattern of CuNi@Ir core-shell nanostructure after etching. (c) HAADF-STEM image and line profile data of hierarchical CuNi@Ir core-shell nanostructure. The yellow arrow in panel (c) indicates line scan direction for the corresponding nanostructure.

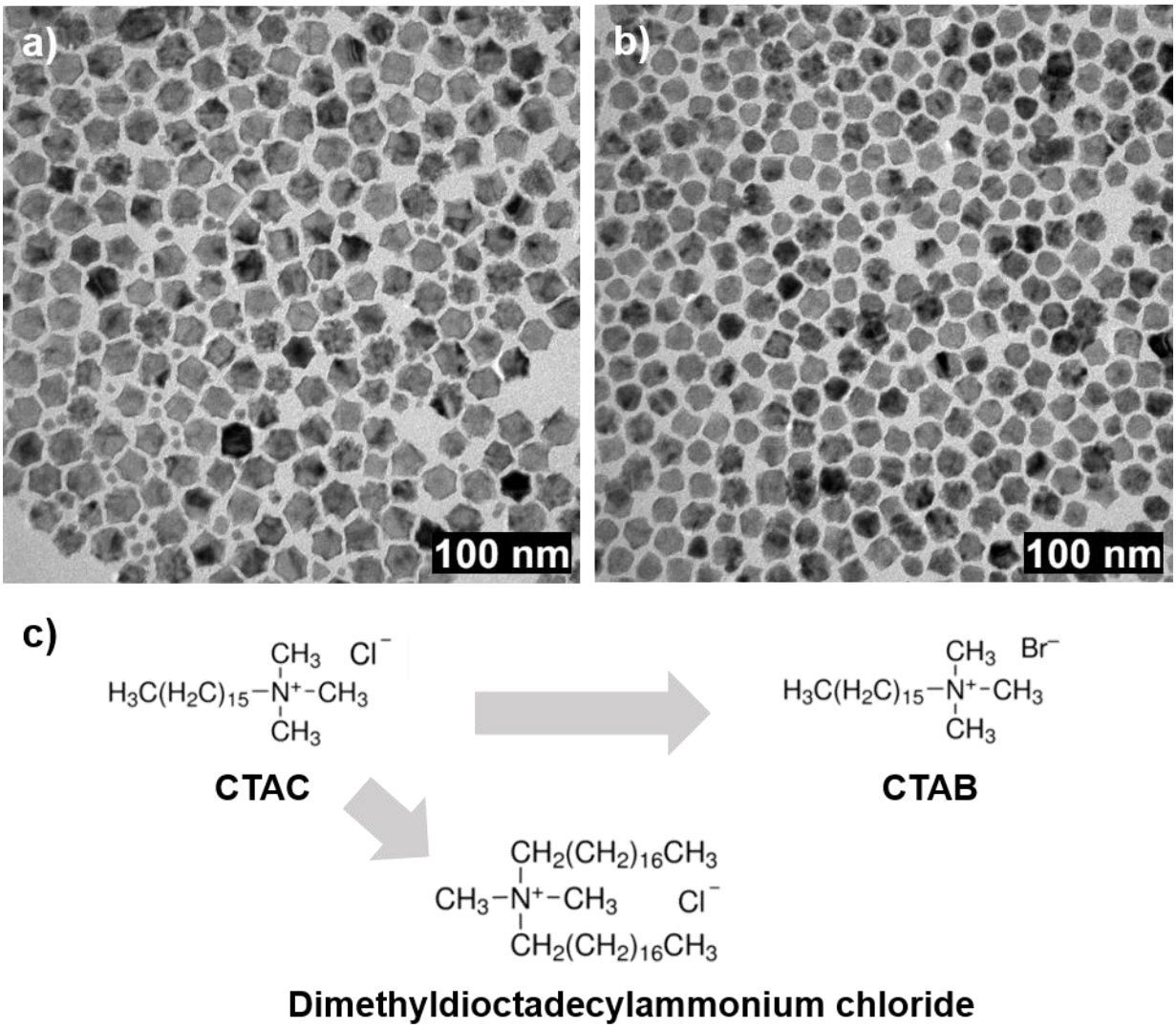

Figure S18. Effect of the type of surfactant on the morphology of unetched nanocrystals. (a,b) TEM images of unetched nanocrystals prepared using (a) cetyltrimethylammonium bromide (CTAB) and (b) dimethyldioctadecylammonium chloride. (c) The chemical structure of CTAC, CTAB, and dimethyldioctadecylammonium chloride.

Table S2. Summary of OER activity parameters of IrNiCu DNF/C, IrNiCu SNF/C, and Ir/C catalysts.

Sample	$\eta_{10,i}$ [a] **(mV)**	j_i **(@ 1.53 V)** [b] **(mA cm^{-2})**	$j_{m,I}$ **(@ 1.53 V)** [c] **(A g$^{-1}_{Ir}$)**
IrNiCu DNF/C	303 ± 4	9.1 ± 1.4	0.46 ± 0.07
IrNiCu SNF/C	306 ± 5	8.1 ± 1.7	0.40 ± 0.09
Ir/C	312 ±3	6.4 ± 0.7	0.32 ± 0.04

Sample	$\eta_{10,f}$ [d] **(mV)**	j_f **(@ 1.53 V)** [e] **(mA cm^{-2})**	$j_{m,f}$ **(@ 1.53 V)** [f] **(A g$^{-1}_{Ir}$)**
IrNiCu DNF/C	302 ± 7	9.5 ± 2.2	0.47 ± 0.11 (0.56 ± 0.13) [g]
IrNiCu SNF/C	318 ± 9	5.5 ± 1.7	0.28 ± 0.08 (0.34 ± 0.10) [g]
Ir/C	326 ± 12	4.4 ± 1.3	0.22 ± 0.06 (0.25 ± 0.07) [g]

[a] Initial overpotential to drive 10 mA cm^{-2}

[b] Initial current density

[c] Initial mass activity

[d] Overpotential to drive 10 mA cm^{-2} after the durability test

[e] Current density after the durability test

[f] Mass activity after the durability test

[g] Mass activity calculated by considering the amount of Ir dissolved during the durability test. The amount was determined by inductively coupled plasma mass spectrometry analysis of the electrolyte after the test.

Table S3. Comparison of experimental conditions, overpotentials, and mass activity IrNiCu **DNF**/C with previously reported catalysts.

Catalysts	Catalyst Description	Ir or IrO_x loading (μg cm^{-2})	Electrolyte	η_{10} (V) [a]	j_m (@ η = 0.30 V) [b] (A $mg^{-1}_{Ir\ or\ IrOx}$)	Ref.
IrNiCu DNF/C	IrNiCu double nanoframe (12.5 wt%)	20	0.1 M $HClO_4$	0.30	0.46 ± 0.07	This Work
Templated IrO_2	Mesoporous IrO_2 film templated by polymer	–	0.1 M $HClO_4$	0.27	–	S1
Ir NPs	2 nm Ir nanoparticles (20 wt%)	10.2	0.1 M $HClO_4$	0.34	0.27	S2
IrO_2 NPs	Rutile IrO_2 nanoparticles (50 wt%)	50	0.1 M $HClO_4$	0.37	0.03	S3
a-IrO_x	Amorphous IrO_x film	<100	1 M H_2SO_4	0.22	20> (extrapolated)	S4
IrO_x-350	IrO_x film annealed at 350 °C	–	0.1 M $HClO_4$	0.32	–	S5
DO-$IrNi_{3.3}$	Electrochemically oxidized $IrNi_x$ nanoparticles (15.3 wt%)	10.2	0.05 M H_2SO_4	0.31	0.62	S6
$IrNiO_x$/Meso-ATO	$IrNiO_x$ core-shell nanoparticles supported on mesoporous ATO (19.3 wt%)	10.2	0.05 M H_2SO_4	0.33	0.30	S7
$Cu_{0.3}Ir_{0.7}O_\delta$	Cu-doped IrO_x (No support)	200	0.1 M $HClO_4$	0.35	0.02	S8
Ir-ND/ATO	Ir nanodendrites on ATO (20 wt%)	10.2	0.05 M H_2SO_4	0.40	0.18	S9
$Cu_{1.11}Ir$	Cu-Ir polyhedral nanocages (No support)	140	0.05 M H_2SO_4	0.29	0.1	S10
Ir-Ni TL/C	Thin layer Ir-Ni core-shell nanoparticles (0.7 wt%)	2	0.05 M H_2SO_4	0.35 (@ 5 mA cm^{-2})	1.2	S11

IrO_x-Ir	IrO_x-Ir core-shell catalysts (No support)	133	0.5 M H_2SO_4	0.295	0.08	S12
3D Ir	3D Ir superstructure (18 wt%)	11.5	0.1 M $HClO_4$	0.27	2.6	S13
$IrO_x/SrIrO_3$	Epitaxially grown $SrIrO_3$ by PLD (Film)	–	0.5 M H_2SO_4	0.275	–	S14
IrO_x/ATO	IrO_x nanoparticles supported on ATO (17.3 wt%)	10.2	0.05 M H_2SO_4	0.36	0.1	S15

[a] Overpotential to drive 10 mA cm^{-2}

[b] Mass activity normalized by Ir or IrO_x loadingf

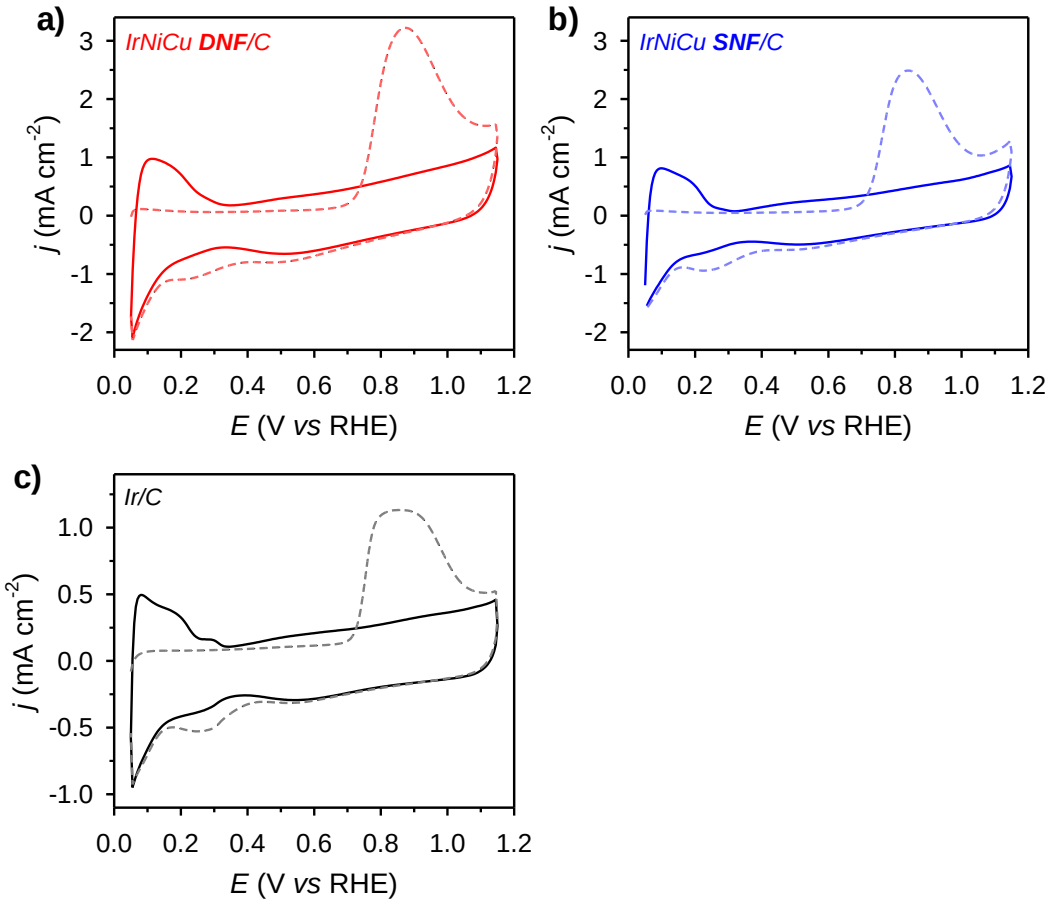

Figure S19. CO-stripping voltammograms (dotted line) and cyclic voltammograms (solid line) for (a) IrNiCu DNF/C, (b) IrNiCu SNF/C, and (c) Ir/C measured in 0.1 M $HClO_4$.

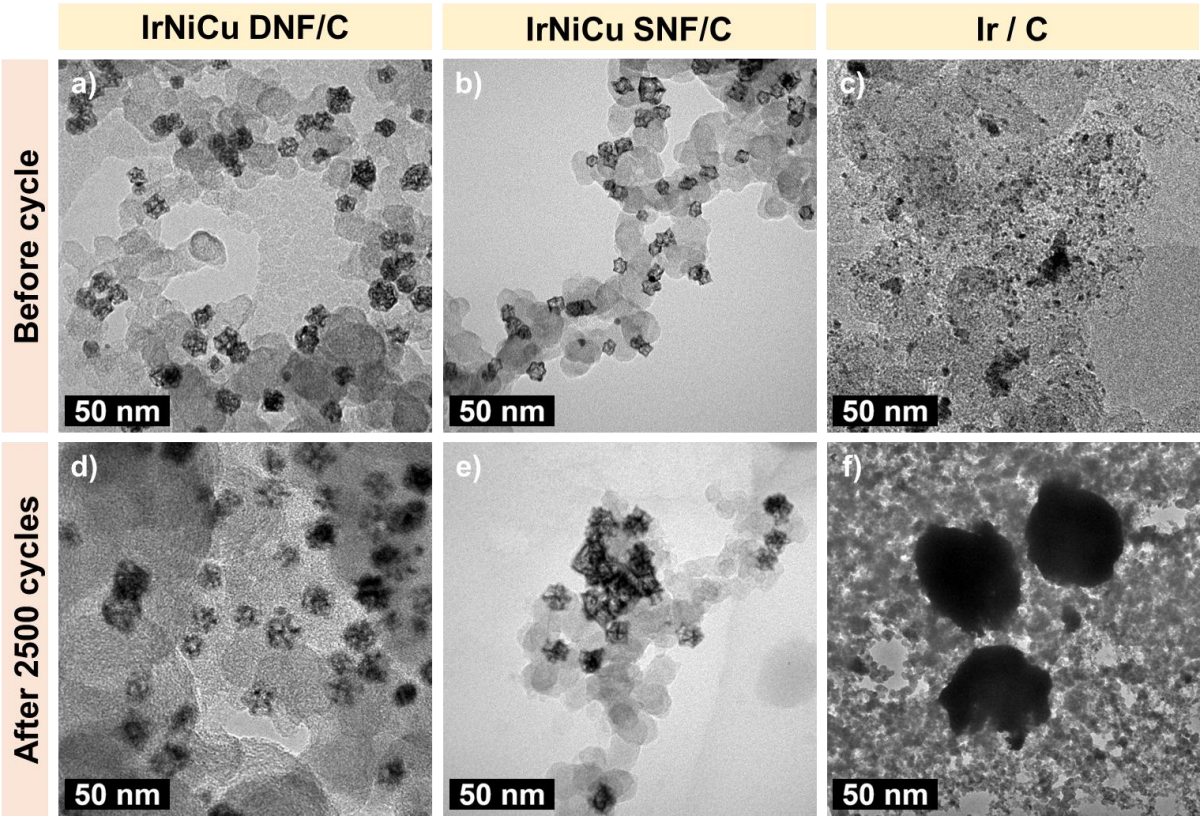

Figure S20. TEM images of (a,d) IrNiCu DNF/C, (b,e) IrNiCu SNF/C and (c,f) Ir/C catalysts before (a–c) and after (d–f) the OER durability test.

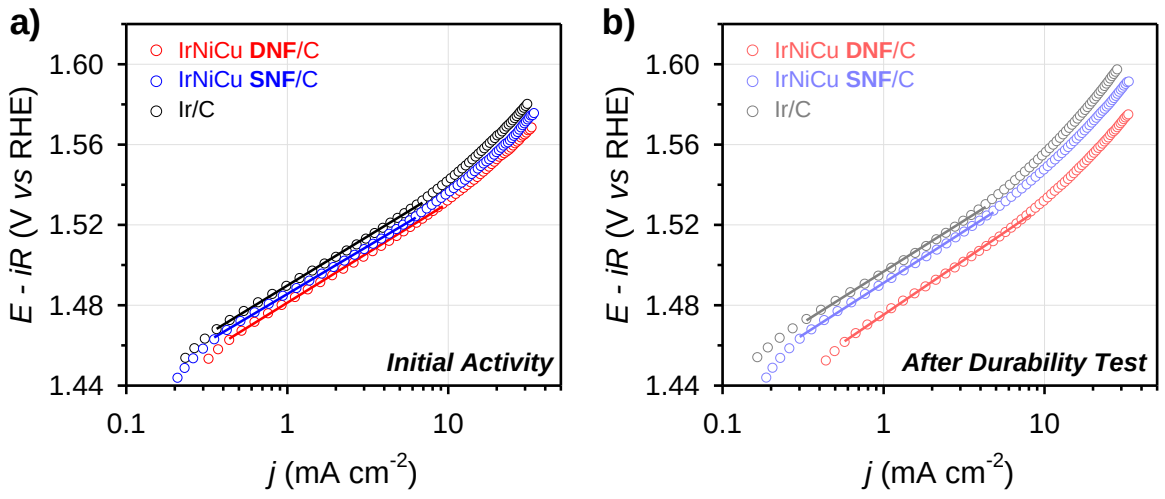

Figure S21. Tafel plots of IrNiCu DNF/C, IrNiCu SNF/C, and Ir/C (a) before and (b) after the OER durability test. Solid lines indicate linear regression lines for estimating Tafel slope.

Table S4. Dissolved amount of Ir from IrNiCu DNF/C, IrNiCu SNF/C, and Ir/C catalysts after the durability test analyzed by ICP-MS that was carried out with the used electrolyte.

Sample	**Dissolved Ir (μg)**	**Percentage of dissolved Ir from the initial mass**	**Dissolved Ir per ECSA (μg cm^{-2}_{Ir})**
IrNiCu DNF/C	0.79	16%	0.12
IrNiCu SNF/C	0.93	19%	0.18
Ir/C	0.59	12%	0.24

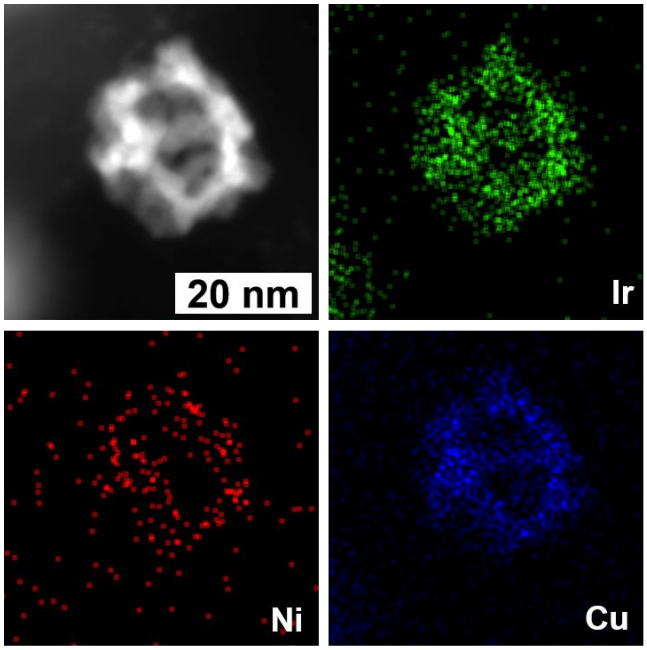

Figure S22. HAADF-STEM image and corresponding elemental mapping images of IrNiCu DNF/C after the OER durability test.

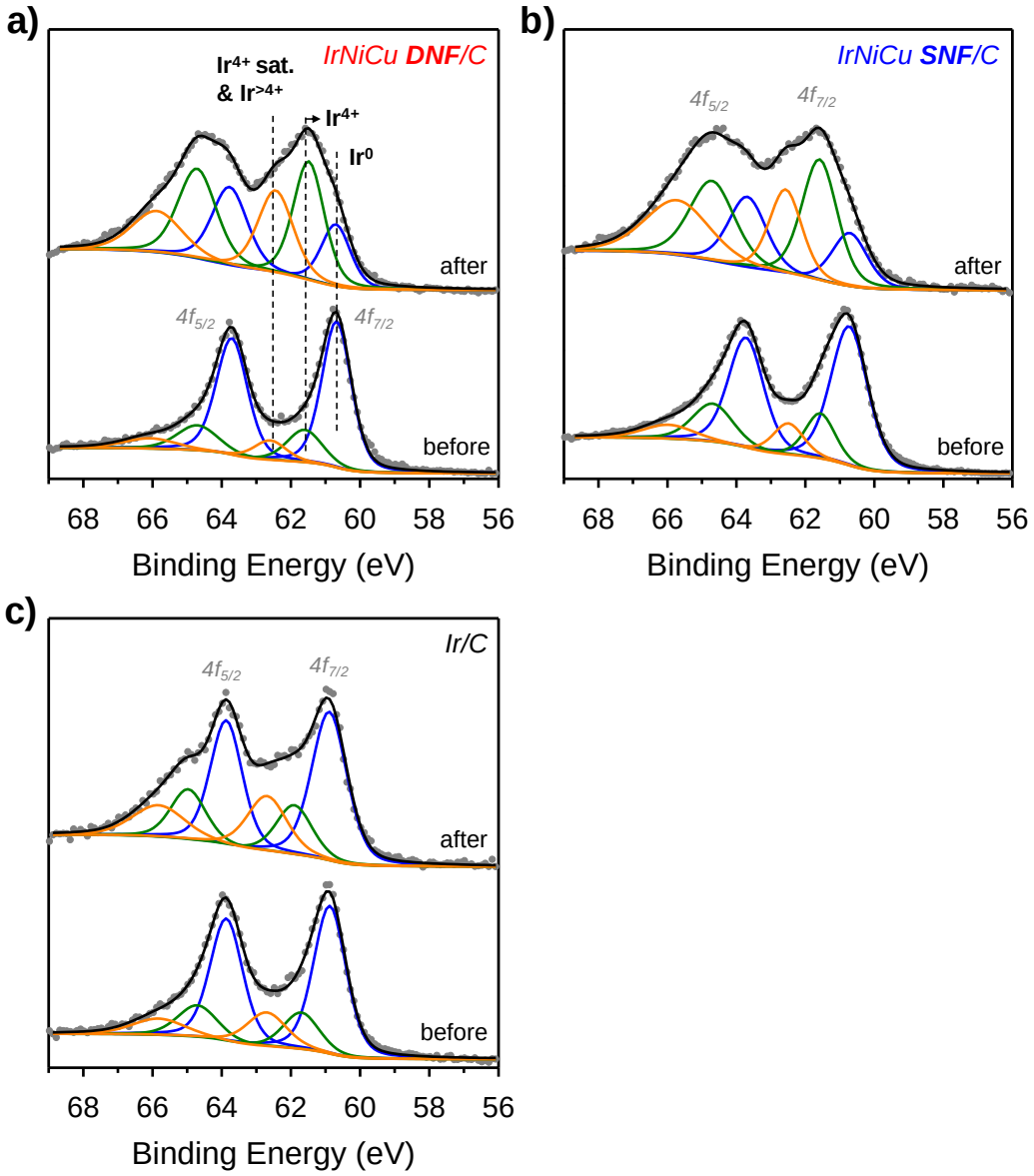

Figure S23. Ir 4f XPS spectra for (a) IrNiCu DNF/C, (b) IrNiCu SNF/C, and (c) Ir/C catalysts before and after the OER durability test.

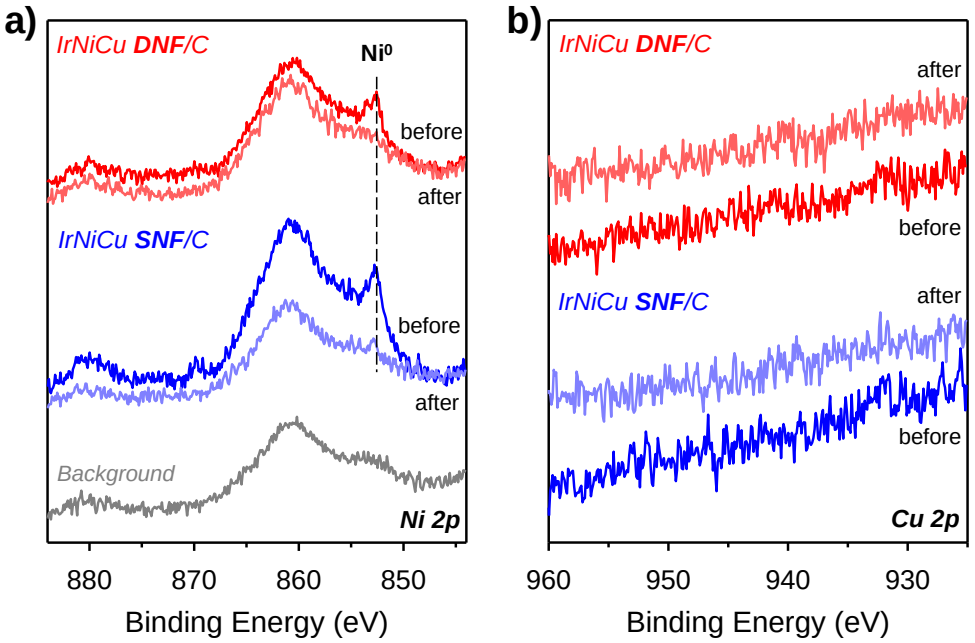

Figure S24. (a) Ni 2p and (b) Cu 2p XPS spectra for IrNiCu DNF/C and IrNiCu SNF/C before and after the OER durability test.

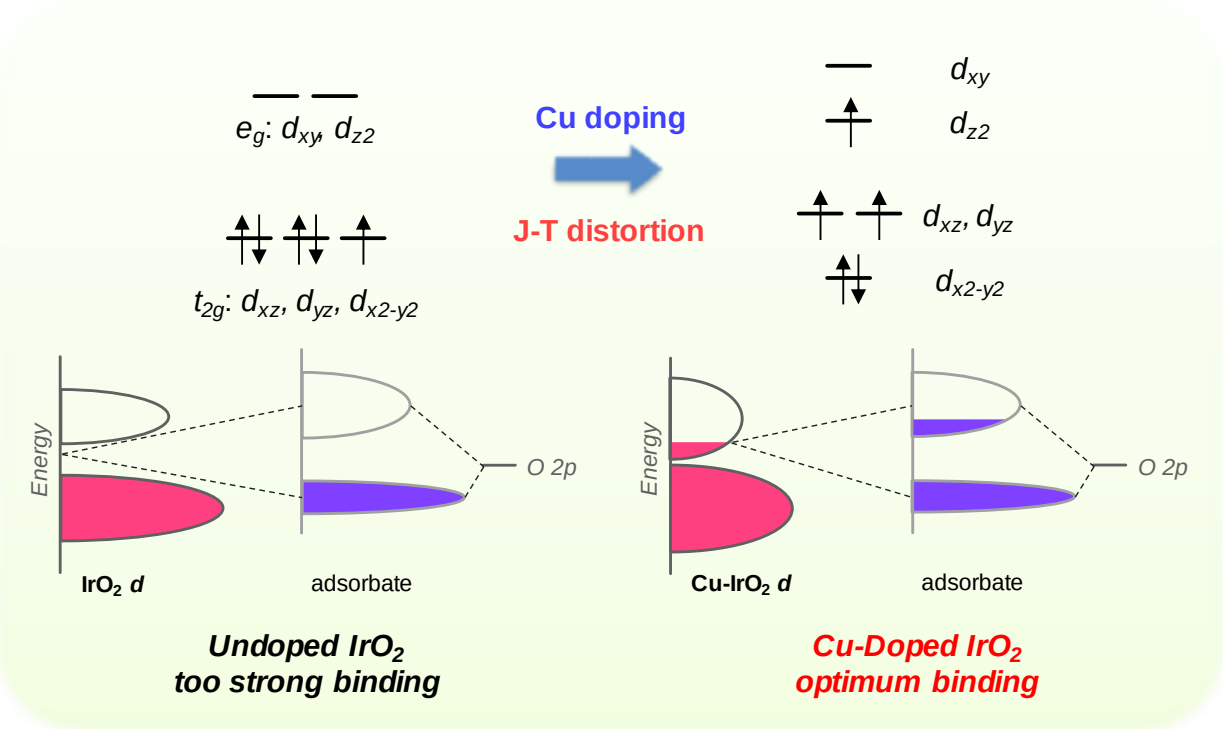

Figure S25. Schematic energy diagram for the binding of un-doped and Cu-doped IrO_2 with oxygen.

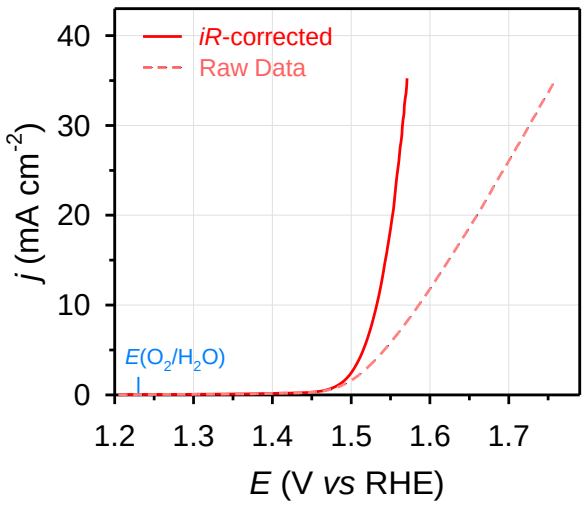

Figure S26. OER polarization curves of IrNiCu DNF/C before and after post *iR*-correction (100%).

References

S1. Ortel, E.; Reier, T.; Strasser, P.; Kraehnert, R. Mesoporous IrO_2 Films Templated by PEO-PB-PEO Block-Copolymers: Self-Assembly, Crystallization Behavior, and Electrocatalytic Performance. *Chem. Mater.* **2011**, *23*, 3201–3209.

S2. Reier, T.; Oezaslan, M.; Strasser, P. Electrocatalytic Oxygen Evolution Reaction (OER) on Ru, Ir, and Pt Catalysts: A Comparative Study of Nanoparticles and Bulk Materials. *ACS Catal.* **2012**, *2*, 1765–1772.

S3. Lee, Y.; Suntivich, J.; May, K. J.; Perry, E. E.; Shao-Horn, Y. Synthesis and Activities of Rutile IrO_2 and RuO_2 Nanoparticles for Oxygen Evolution in Acid and Alkaline Solutions. *J. Phys. Chem. Lett.* **2012**, *3*, 399–404.

S4. Smith, R. D. L.; Sporinova, B.; Fagan, R. D.; Trudel, S.; Berlinguette, C. P. Facile Photochemical Preparation of Amorphous Iridium Oxide Films for Water Oxidation Catalysis. *Chem. Mater.* **2014**, *26*, 1654–1659.

S5. Reier, T.; Teschner, D.; Lunkenbein, T.; Bergmann, A.; Selve, S.; Kraehnert, R.; Schlögl, R.; Strasser, P. Electrocatalytic Oxygen Evolution Reaction on Iridium Oxide Model Film Catalysis: Influence of Oxide Type and Catalyst Substrate Interactions. *J. Electrochem. Soc.* **2014**, *161*, F876–F882.

S6. Nong, H. N.; Gan, L.; Willinger, E.; Teschner, D.; Strasser, P. IrO_x Core-Shell Nanocatalysts for Cost- and Energy-Efficient Electrochemical Water Splitting. *Chem. Sci.* **2014**, *5*, 2955–2963.

S7. Nong, H. N.; Oh, H.-S.; Reier, T.; Willinger, E.; Willinger, M.-G.; Petkov, V.; Teschner, D.; Strasser, P. Oxide-Supported $IrNiO_x$ Core-Shell Particles as Efficient, Cost-Effective, and Stable Catalysts for Electrochemical Water Splitting. *Angew. Chem., Int. Ed.* **2015**, *54*, 2975–2979.

S8. Sun, W.; Song, Y.; Gong, X.-Q.; Cao, L.; Yang, J. An Efficiently Tuned *d*-Orbital Occupation of IrO_2 by Doping with Cu for Enhancing the Oxygen Evolution Reaction Activity. *Chem. Sci.* **2015**, *6*, 4993–4999.

S9. Oh, H.-S.; Nong, H. N.; Reier, T.; Gliech, M.; Strasser, P. Oxide-Supported Ir Nanodendrites with High Activity and Durability for the Oxygen Evolution Reaction in Acid PEM Water Electrolyzers. *Chem. Sci.* **2015**, *6*, 3321–3328.

S10. Wang, C.; Sui, Y.; Xiao, G.; Yang, X.; Wei, Y.; Zou, G.; Zou, B. Synthesis of Cu–Ir Nanocages with Enhanced Electrocatalytic Activity for the Oxygen Evolution Reaction. *J. Mater. Chem. A* **2015**, *3*, 19669–19673.

S11. Lim, J.; Yang, S.; Kim, C.; Roh, C.-W.; Kwon, Y.; Kim, Y.-T.; Lee, H. Shaped Ir–Ni Bimetallic Nanoparticles for Minimizing Ir Utilization in Oxygen Evolution Reaction. *Chem. Commun.* **2016**, *52*, 5641–5644.

S12. Lettenmeier, P.; Wang, L.; Golla-Schindler, U.; Gazdzicki, P.; Cañas, N. A.; Handl, M.; Hiesgen, R.; Hosseiny, S. S.; Gago, A. S.; Friedrich, K. A. Nanosized IrO_x–Ir Catalyst with

Relevant Activity for Anodes of Proton Exchange Membrane Electrolysis Produced by a Cost-Effective Procedure. *Angew. Chem., Int. Ed.* **2016**, *55*, 742–746.

S13. Pi, Y.; Zhang, N.; Guo, S.; Guo, J.; Huang, X. Ultrathin Laminar Ir Superstructure as Highly Efficient Oxygen Evolution Electrocatalysts in Broad pH Range. *Nano Lett.* **2016**, *16*, 4424–4430.

S14. Seitz, L. C.; Dickens, C. F.; Nishio, K.; Hikita, Y.; Montoya, J.; Doyle, A.; Kirk, C.; Vojvodic, A.; Hwang, H. Y.; Norskov, J. K.; Jaramillo, T. F. A Highly Active and Stable $IrO_x/SrIrO_3$ Catalyst for the Oxygen Evolution Reaction. *Science* **2016**, *353*, 1011–1014.

S15. Oh, H.-S.; Nong, H. N.; Reier, T.; Bergmann, A.; Gliech, M.; de Araújo, J. F.; Willinger, E.; Schlögl, R.; Teschner, D.; Strasser, P. Electrochemical Catalyst-Support Effects and Their Stabilizing Role for IrO_x Nanoparticle Catalysts during the Oxygen Evolution Reaction. *J. Am. Chem. Soc.* **2016**, *138*, 12552–12563.